Influence of active metal loading and oxygen mobility on coke-free dry reforming of Ni–Co bimetallic catalysts

Petar Djinović [a,b,*], Ilja Gasan Osojnik Črnivec [a], Boštjan Erjavec [a,b], Albin Pintar [a,b]

[a] Laboratory for Environmental Sciences and Engineering, National Institute of Chemistry, Hajdrihova 19, SI-1001 Ljubljana, Slovenia
[b] Center of Excellence "Low Carbon Technologies", Hajdrihova 19, SI-1001 Ljubljana, Slovenia

ABSTRACT

Two different techniques (precipitation with ammonia and hydrothermal synthesis with ethylene glycol, both followed by autoclave aging) were employed for the synthesis of CeO_2–ZrO_2 mixed oxides on a 80–20 wt.% basis. Aging parameters, such as time and temperature, were systematically investigated in order to determine the optimal conditions to maintain high surface area and oxygen mobility of the prepared solids. Different loadings of nickel and cobalt (3, 6, 12 and 18 wt.%) were subsequently deposited via homogeneous deposition precipitation method. Calcined bimetallic catalysts were characterized by N_2 adsorption–desorption, XRD, H_2-TPR, TPO-TGA and FE-SEM methods, and tested for activity, selectivity and stability in the reforming of equimolar CH_4–CO_2 gas streams. During temperature programmed methane reforming tests, syngas with a H_2/CO ratio between 0.3 and 0.79 was produced. Growth of carbon nanofilaments over the catalyst does not lead to deactivation, but can cause reactor plugging. Two conditions are vital and must be fulfilled simultaneously to avoid excessive carbon deposition: strong interaction between the NiCo bimetallic particles and CeZr support, which exists only at NiCo loadings up to 6 wt.%, as well as high oxygen mobility within the highly defective CeO_2–ZrO_2 crystalline lattice for timely carbon oxidation.

1. Introduction

Biogas represents a source of methane and carbon dioxide of ever increasing importance, since different redundant organic materials (waste streams originating from agricultural activity as well as municipal origin), or purpose-grown energy crops are being dedicated for transformation into this energy-rich gas mixture [1]. Biogas production in Europe has grown exponentially in the last decade, with 10 billion m^3 of biomethane produced in the year 2009, and projected 46 billion m^3 biomethane primary energy potential in 2020 [2]. Biogas can be used directly as an individual source of either CH_4 or CO_2, naturally, after appropriate purification (adsorption of trace impurities and pressure swing adsorption for CO_2 removal) [3].

Combustion of methane, isolated from biogas, could represent an alternative to natural gas and thus decrease dependence of today's energy demanding population and economy on fossil fuels [4]. Another possibility for biogas valorization is its catalytic transformation into syngas, either by steam reforming or partial

oxidation processes [5,6]. These well established technologies have both advantages and drawbacks. For example, partial oxidation is appropriate also for reforming of heavy hydrocarbons and naphtha and produces syngas with a H_2/CO ratio below 2. It does not require desulphurization step, but a cryogenic air separation unit is needed for oxygen production. Steam reforming process on the other hand requires a desulphurization unit, it faces steam corrosion issues, but produces syngas with a H_2/CO ratio of roughly 3, which is very beneficial for pure hydrogen production [7].

Methane dry reforming (MDR) reaction (Eq. (1)), uses CO_2 as an oxidizing agent, much like O_2 or H_2O in partial oxidation and steam reforming reactions, respectively [8]. Consequently, purified biogas can be used directly acting as a feedstock for the MDR reaction. It performs its task in being a part of a complementary strategy to reduce/solve the enormous problem of our fossil fuel based society [1].

$$CH_4 + CO_2 \leftrightarrow 2H_2 + 2CO, \quad \Delta H^\circ{}_{298\,K} = 247\,kJ/mol \qquad (1)$$
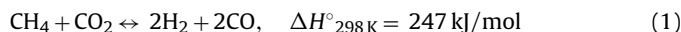
The reaction is strongly endothermic (247 kJ/mol, compared to methane steam reforming with reaction enthalpy of 206 kJ/mol [9]) and requires high temperatures to achieve noticeable CH_4 and CO_2 conversions and a beneficial H_2/CO ratio. The latter in ideal cases can reach unity, but practical operating conditions are strongly influenced by the co-occurrence of reverse water gas shift (RWGS)

* Corresponding author at: Laboratory for Environmental Sciences and Engineering, National Institute of Chemistry, Hajdrihova 19, SI-1001 Ljubljana, Slovenia. Tel.: +386 1 47 60 249; fax: +386 1 47 60 460.
E-mail address: petar.djinovic@ki.si (P. Djinović).

reaction (Eq.(2)), which is quasi equilibrated in a wide range of operating conditions and strongly decreases the H_2 yield [10].

$$H_2 + CO_2 \leftrightarrow H_2O + CO, \quad \Delta H°_{298\,K} = 41\,kJ/mol \qquad (2)$$
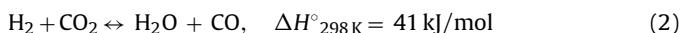
To minimize the contribution of the RWGS reaction and to improve the H_2 yield, high temperatures (>1023 K), or a CH_4/CO_2 ratio well above 1 are required [11].

High-temperature operation requires use of special materials for reactor design, not to mention soaring energy consumption for achieving the desired reaction conditions. On the other hand, by operating in the methane rich regime (CH_4/CO_2 molar ratio in biogas is usually between 1 and 3), carbon deposition over the catalyst is strongly enhanced, which renders transition metal catalysts useless, as a result of their fast carbon accumulation [8]. A possible solution lies in the utilization of carbon resistant Ru and Rh based reforming catalysts [12–15], but these are unsuitable for large-scale industrial applications due to their high price. Another drawback of using a large surplus of methane in the feed is the need to separate and recycle the gas stream discharged from the reactor, since the limiting reactant (CO_2) will be consumed, with a substantial fraction of methane still remaining unconverted.

Consequently, great potential lies in the development of an active, carbon-resistant transition metal catalyst, which is capable of reforming real biogas streams. Major improvements toward minimizing carbon accumulation over nickel based catalysts were achieved (nickel is generally accepted as the most active among the transition metals for methane activation [16]) via the following pathways:

(i) Alloying nickel with cobalt, addition of tin. Alloying nickel with cobalt breaks the integrity of surface nickel ensembles, which decreases the apparent nickel particle size to the extent, which is too small for carbon nucleation and growth. Additionally, formation of NiCo alloy is reported to improve catalyst stability by improving resistance of active metal oxidation [17].

Addition of tin causes the rate determining methane activation step to shift from most active low-coordinated to less active well-coordinated Ni sites, which increases the activation barriers for methane dissociation. It also weakens the binding strength of carbon atoms to the most active low-coordinated sites, which is a requirement for the carbon nucleation at these sites [18]. Because nickel surface is decorated with tin, active-sites are partially blocked, which also decreases the catalytic activity. Hou et al. [16] attributed higher dispersion of nickel in the presence of tin, improvement of nickel reducibility and better resistance to sintering.

(ii) Use of metal oxide catalyst support, which exhibits good redox properties and oxygen mobility, such as CeO_2, CeO_2–ZrO_2, YSZ, TiO_2 and various doped CeO_2 supports. Numerous authors report that CeO_2 may promote metal dispersion and prevent sintering. This promotion is associated with strong metal–ceria interaction, its oxygen storage capacity and Ce^{4+}/Ce^{3+} redox properties. CeO_2–ZrO_2 solid solution exhibits good thermal stability and superior oxygen mobility, compared to CeO_2 alone. This is due to its highly defective structure (zirconium incorporation into ceria crystalline lattice) and consequently facile oxygen vacancy formation, which are active sites for the dissociative adsorption of CO_2. High dispersion of active metal phase is a prerequisite for good metal support interaction and high oxygen mobility is the prevailing mechanism for effective oxidation of carbon deposits, formed over active metal surface via oxygen spillover [17,19,20].

(iii) Doping with alkali metals such as potassium, calcium and magnesium [21] is believed to increase the basicity of the catalyst and increase the surface coverage with hydroxyls via RWGS reaction, which is beneficial for carbon gasification. Alkalized

nickel catalysts with potassium are reported with lower sticking probability for methane, compared to undoped catalysts [22], which reduces the number of nickel active sites for methane decomposition. Addition of Ca is reported to improve interaction of nickel with support, which slows down sintering. However, positive effect of calcium addition depends on its loading and properties of the support [23]. Improvement of coking resistance by alkali metal doping is generally associated with catalyst deactivation due to partial active site blocking.

In this work, various loadings of Ni and Co were dispersed over reducible CeO_2–ZrO_2 solid solutions. Different synthesis methods and aging conditions were systematically tested in order to isolate the optimal conditions for preparation of thermally stable and highly reducible CeO_2–ZrO_2 solid solutions. The effect of nickel and cobalt loading on activity and stability was evaluated. Coking characteristics of these catalysts were also analyzed. Synthesis method and chemical composition of prepared catalysts were steered toward its minimization while maintaining stable catalytic performance.

2. Experimental

CeO_2–ZrO_2 mixed oxide catalyst supports (80:20 by weight) were synthesized using either ethylene glycol [24] (in the following text denoted as CeZr EG), or hydrothermal method using NH_4OH as the precipitating agent (denoted as CeZr HT).

During a typical EG synthesis, 1 g of cerium (III) nitrate hexahydrate (Fluka, p.a.) and zirconium (IV) oxynitrate hydrate (Sigma Aldrich, >99% purity) were dissolved in 1 ml of ultrapure water and mixed with 1 ml of propionic acid (Merck, >99% purity) and 30 ml of ethylene glycol (Merck, >99% purity). The solution was transferred to PTFE-clad autoclaves and aged for 3.3, 6.7 or 10 h at 180 or 200 °C. After the appointed aging period, the precipitated solids were separated from the esterified solution by centrifugation at 8950 rpm in 15 min cycles. The obtained solid was washed with ultrapure water and ethanol and dried overnight in a laboratory drier at 70 °C.

During the HT method, cerium (III) nitrate hexahydrate and zirconium (IV) oxynitrate hydrate were dissolved in 100 ml of ultrapure water. The solution was added drop-wise to 250 ml of 25% aqueous ammonia solution (Merck, p.a.) while stirring intensively using a magnetic stirrer. The obtained suspension was transferred to PTFE-clad autoclaves and aged for 6, 12, 26, 48 and 90 h at various temperatures: 100, 120, 140 and 160 °C. The aged product was filtered, consecutively washed with distilled water and ethanol and dried overnight in a laboratory drier at 70 °C.

After drying, the CeZr HT and CeZr EG powders were calcined for 4 h at 400 °C in air with the heating ramp of 5 °C/min. Such a calcination temperature was selected in order to maintain the initial specific surface area of the CeZr support as high as possible as well as to accommodate highly dispersed NiCo phase during the subsequent deposition step. During the preliminary experiments (not included in the manuscript), the CeZr EG support was calcined at temperatures up to 800 °C, which resulted in a substantial decrease of BET specific surface area. This resulted in much higher degree of NiCo phase aggregation (and consequently larger NiCo particle size) during subsequent NiCo deposition.

Nickel and cobalt, originating from nitrate precursors (Merck, p.a.), were deposited at the 40:60 weight ratio using homogeneous deposition precipitation method, which is in-depth described by de Jong [25].

Briefly, urea (Merck, p.a.) was used to increase the pH value of the aqueous CeZr suspension in a slow, controlled manner, while being heated from room temperature to 90 °C under reflux. This temperature was maintained for 22 h in order to allow sufficient

time for nickel and cobalt deposition. Afterwards, the suspension was filtered, washed with ethanol and water, and dried overnight in air at 70 °C. NiCo/CeZr catalysts were thermally stabilized by 4 h calcination at 650 °C in air. Total loadings of nickel and cobalt (3, 6, 12 and 18 wt.%) were deposited over the CeZr support, which are in the following denoted as xNiCo EG or xNiCo HT. Letter x represents the total active metal content while EG or HT indicates the synthesis method, used for the preparation of CeZr support.

Catalyst samples were thoroughly characterized by XRD (X'pert Pro by Panalytical), N_2 sorption (Tristar II 3020 by Micromeritics), H_2-temperature programmed reduction and CO chemisorption (AutoChem II 2920 by Micromeritics) methods. Prior to H_2-TPR measurements, all samples were degassed in situ in a flow of nitrogen (50 Nml/min) while heated from RT to 300 °C, followed by an isothermal step (60 min at 300 °C). After pretreatment, the temperature was lowered to 50 °C in nitrogen flow, followed by a 15 min stabilization period. H_2-TPR analysis was performed using 50 Nml/min of 5% H_2/N_2 mixture from RT to 800 °C with a 5 °C/min ramp, followed by 10 min isothermal step. Hydrogen consumption during the performed tests was evaluated from integration of H_2 peaks. Types and amounts of deposited carbon over spent catalysts were determined using TPH and TPO/TGA (Pyris 1 by Perkin Elmer), CHNS elemental analysis (2400 series II analyzer by Perkin Elmer) and FE-SEM/EDX microscopy (Supra 35 VP).

Prior to all catalytic tests, powdered catalyst samples were reduced in situ in a 20% H_2/N_2 mixture (50 Nml/min) by heating from RT to 750 °C with a 10 °C/min ramp, followed by an isothermal step at 750 °C for 1 h. After reduction, temperature was lowered to 500 °C in the equimolar CH_4/CO_2 atmosphere, which served as the initial activity testing temperature.

Catalytic tests were performed using a Microactivity Reference reactor system (MARef from PID Eng&Tech) equipped with a tubular quartz reactor (I.D. = 10 mm). Reactor feed comprised of an undiluted equimolar gaseous stream of CH_4 and CO_2 at 50 NmL/min each. Absolute operating pressure was maintained at 1.2 bar during all tests. Catalyst bed comprised of 150 mg catalyst, diluted with 850 mg of SiC sand (0.2–0.5 mm, BET surface area 0.03 m^2/g), which was fixed between two quartz wool flocks (WHSV = 37 L/$g_{cat.}$ h). A K-type thermocouple was positioned inside the catalyst bed for accurate temperature acquisition. Each temperature increment was monitored for 2.5 h and the gases leaving the reactor were fed through a heated capillary (1/8 in. at 200 °C) to the GC (7890A, Agilent Technologies), where quantitative and qualitative composition of reactor outlet stream was determined. Isothermal methane dry reforming tests at 550 and 750 °C were performed using identical operating conditions, with the only difference being 500 mg of catalyst used.

3. Results and discussion

3.1. CeO₂–ZrO₂ catalyst support

CeZr mixed oxide catalyst supports, prepared using EG and HT methods and digested under various conditions, prior to the deposition of nickel and cobalt were characterized by N_2 adsorption/desorption, XRD and H_2-TPR techniques.

H_2-TPR profiles of CeZr HT and CeZr EG solid solutions are presented in Fig. 1 and reveal substantially different behavior of both materials. Generally, reduction of CeO_2 takes place via a stepwise mechanism: first reduction of the outermost layers of Ce^{4+} occurs (reducible surface-capping oxygen of ceria at around 400–550 °C), followed by the reduction of the inner Ce^{4+} layer (bulk oxygen), causing the high-temperature signal at around 750–850 °C [26]. However, H_2-TPR profile of CeZr solid solution is different. Incorporation of isovalent non-reducible elements like Zr^{4+} into CeO_2
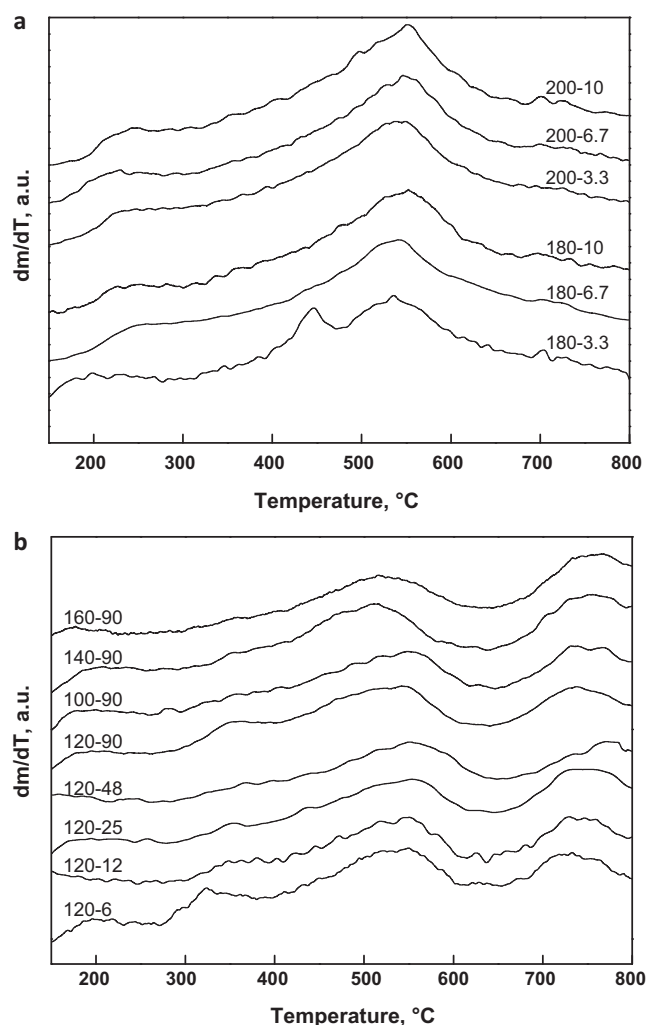

Fig. 1. (a) H_2-TPR profiles of CeZr EG solid solutions, aged at different temperatures and times; (b) H_2-TPR profiles of CeZr HT solid solutions, aged at different temperatures and times.

lattice positively influences the oxygen mobility and oxygen storage capacity in the crystalline lattice of the CeZr solid solution and shifts hydrogen consumption toward lower temperatures. Deformation of metal–oxygen bonds (due to different Ce^{4+} and Zr^{4+} ionic radii, which causes lattice distortion and favors structural defects) results in highly mobile lattice oxygen species, so that the reduced zone is not confined to the surface layers, but extends deep into the bulk [27]. Mamontov et al. [28] suggest that incorporation of the smaller Zr^{4+} ion gives rise to strain in the structure of mixed oxide, which can be alleviated by the promotion of Ce^{4+} to Ce^{3+} ions (ionic radius of 97 vs. 128 pm, respectively). Formation of a CeO_2–ZrO_2 solid solution results in a shift of bulk reduction downwards to about 550–650 °C [29].

The high oxygen mobility of CeZr EG solids led to the identification of single broad reduction feature starting at around 300 °C, centered at 535–555 °C and slowly fading toward the end-temperature of 800 °C. Despite noticeable differences in the extent of lattice oxygen removed during the performed H_2-TPR experiments on CeZr EG materials (Table 1), the CeZr EG sample aged for 3.3 h at 180 °C was unique, exhibiting two overlapping reduction peaks, centered at 447 and 535 °C, respectively (Fig. 1a). Since BET specific surface area of this sample was highest among all (120.9 m^2/g) and also its surface to bulk ratio, we can say with high probability that low temperature reduction peak is a

Table 1
Specific surface area, average CeO$_2$–ZrO$_2$ crystallite size, calculated from XRD data and percentage of CeO$_2$ reduced during H$_2$-TPR analysis for various calcined CeZr HT and CeZr EG samples, calcined 4 h at 400° C in air.

Sample	BET surface area (m^2/g)	Average CeO$_2$–ZrO$_2$ crystallite size (nm)	Transformation of Ce^{4+} to Ce^{3+} (%)
CeZr HT 100-90	64.6	32.2	44.5
CeZr HT 120-6	66.5	34.9	50.5
CeZr HT 120-12	58.6	34.5	48.1
CeZr HT 120-25	54.4	40.9	42.7
CeZr HT 120-48	52.1	42.7	43.7
CeZr HT 120-90	73.9	25.1	49.1
CeZr HT 140-90	58.9	34.9	42.1
CeZr HT 160-90	47.5	36.1	39.6
CeZr EG 180-3.3	120.9	5.4	67.4
CeZr EG 180-6.7	109.2	5.5	59.8
CeZr EG 180-10	68.2	5.6	48.5
CeZr EG 200-3.3	82.4	5.7	59.2
CeZr EG 200-6.7	71.0	5.8	59.0
CeZr EG 200-10	71.3	5.7	59.6

consequence of hydrogen consumption due to the most facile reduction of surface layer of CeZr EG support.

Progress of hydrogen-induced temperature programmed reduction of CeZr HT samples (Fig. 1b) was noticeably different compared to CeZr EG materials. Generally, two broad peak could be discerned, the first one centered at around 500–550 °C and the second one at around 750 °C. The measured H$_2$-TPR profiles are remarkably similar to the reduction profile of pure ceria, which exhibits two well separated peaks, belonging to reduction of its surface and bulk, respectively. As mentioned earlier, based on the position of the main diffraction maximum of CeZr HT material, XRD analysis confirmed high similarity of its structure to pure CeO$_2$, which would predict the temperature programmed reduction to proceed with similar dynamics. Additionally, this indicates that zirconium incorporation into the host CeO$_2$ structure was less efficient during HT synthesis. The effectiveness of CeZr solid solution formation originates from the synthesis method used, since the formation of precipitate using HT and EG synthesis methods occurs via completely different pathways. During the addition of NH$_4$OH using HT method, the precipitate consisting of cerium and zirconium hydroxides is formed and its homogenization takes place via continuous dissolution and re-precipitation during hydrothermal aging. On the other hand, during the EG synthesis method, dissolved cerium and zirconium nitrate precursors, ethylene glycol and propionic acid form a gel, which consists of more efficiently coupled cerium and zirconium species.

Beside the two main reduction features at 550 and 750 °C, a shoulder at around 340 °C was observed during analysis of CeZr HT mixed oxides, which correlated with increasing specific surface area (CeZr HT 120-90 > CeZr HT 120-6 > CeZr HT 120-12 > CeZr HT 120-25 > CeZr HT 120-48) and thus indicating it is a surface relating phenomenon. Similar behavior was observed by Laachir et al. [30] during H$_2$-TPR analysis of high surface area CeO$_2$. These authors ascribed it to desorption of surface hydroxyls in the form of water vapor. The low temperature shoulder was not observed by these authors during H$_2$-TPR analysis of low surface area CeO$_2$.

During H$_2$-TPR analysis of CeZr materials (Table 1), substantially higher extent of reduction was achieved over CeZr EG samples (up to 67.4% of total Ce^{4+} transformed to Ce^{3+}), compared to CeZr HT (up to 50.5% of total Ce^{4+} transformed to Ce^{3+}). This is likely connected to smaller crystallite size and consequently shorter diffusion path of oxygen from the material bulk to the surface (consistent with the kinetic model, which assumes that high temperature reduction process is controlled by slow diffusion of oxygen vacancies from bulk to the oxide surface [31]), as well as more distorted CeO$_2$

lattice of the CeZr EG material due to higher degree of Zr^{4+} incorporation, which was previously reported to be crucial for enabling high oxygen mobility [32].

Specific surface areas of differently aged CeZr EG and CeZr HT supports, measured using BET method are presented in Table 1. If we first consider CeZr EG solid solutions aged at 180 °C, a continuous decrease of specific surface area and oxygen mobility can be observed with prolonging aging time, coupled with a small, but steady increase of CeO$_2$ crystallite size. A clear correlation between high BET specific surface area, small crystallite size and high oxygen mobility can be identified for CeZr EG solid solutions. Higher surface to volume ratio of nanosized CeZr particles enables a more complete reduction during the temperature programmed reduction tests, indicating a possibility of progressive reduction from the surface inwards [31].

When comparing CeZr EG solid solutions aged at 200 °C, steady values of BET surface area, crystallite size and oxygen mobility were observed from 6.7 h of aging onward, confirming that ripening/aging process of CeZr particles occurs faster at higher temperatures and that a thermodynamically stable steady state is presumably achieved. Among all synthesis conditions, CeZr EG support aged 3.3 h at 180 °C was selected for further impregnation with nickel and cobalt and all subsequent catalytic testing due to its highest specific surface area and most pronounced oxygen mobility.

During the systematic investigation of HT synthesis method conditions [33], aging time was fixed at 90 h and different aging temperatures were investigated (100, 120, 140 and 160 °C). As presented in Table 1, material aged at 120 °C clearly exhibited the highest oxygen mobility, specific surface area and smallest crystallite size.

In the second stage of material synthesis optimization, the influence of aging time (6–90 h) on morphology of CeZr mixed oxides at the aging temperature of 120 °C was studied.

Previous studies on hydrous zirconia showed that temperature, pH value and length of hydrothermal treatment affects the surface area, porosity and thermal stability of the resulting zirconia [33,34]. It was postulated that as a result of the high temperatures during hydrothermal synthesis, collisions between primary particles are enhanced, which leads to the formation of a porous matrix of nanoparticles, which is further strengthened by the continuous dissolution and re-precipitation of material under hydrothermal conditions. The pH value of the reaction medium determines the solubility of the hydrous oxide and consequently the extent of dissolution and re-precipitation of the material. Increased thermal stability of the hydrothermally treated nanomaterials may be due to the decreased number of defect sites, which are believed to be responsible for sintering of particles.

It can be seen from data listed in Table 1 that increasing the aging time from 6 to 48 h leads to a continuous ordering of the CeZr crystalline structure, which is evident from a continuous decrease in specific surface area, average crystallite size and oxygen mobility. The CeZr HT mixed oxide, aged for the longest time (90 h), exhibited the highest specific surface area and oxygen mobility very similar to the values measured over sample, aged for 6 h. Since no gain in oxygen mobility and only minor improvement of BET specific area could be benefited from increasing aging time at 120 °C, the CeZr HT support aged 6 h at 120 °C was selected for impregnation with nickel and cobalt and further catalytic tests.

SEM characterization of the calcined CeZr supports (Fig. 2) was performed to inspect their morphology. The CeZr HT mixed oxide was found to be constituted of round nanoparticles, which were between 20 and 30 nm in size and aggregated into porous structures with dimensions up to several micrometers. The size of nanoparticles coincides well with the dimensions, calculated from XRD data (Table 1).
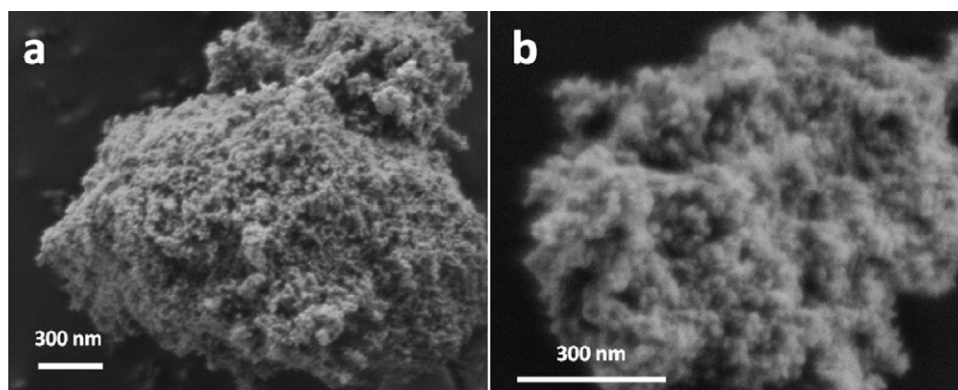
Fig. 2. SEM micrographs of (a) CeZr EG and (b) CeZr HT mixed oxide supports.

Crystallite dimensions between 10 and 15 nm were identified for the CeZr EG supports using SEM microscopy, whereas XRD data predicted this value to be below 6 nm. The discrepancy very likely originates from highly defective crystalline structure of these nanopowdered materials. Defective structures also result in poorer scattering of the incident X-ray light, leading to apparent broadening of the diffraction peaks and consequently substantial underestimation of their size [35].

Results of XRD analysis of CeZr HT and CeZr EG catalyst supports are presented in Fig. 3.

A shift of diffraction peak positions toward higher 2θ values was observed for all synthesized CeZr supports (28.555° in CeO_2 standard (PDF 00-034-0394), 28.618° and 28.886° for CeZr HT and CeZr EG, respectively). The latter value correlates closely with the position of the FCC CeO_2 (1 1 1) diffraction maximum of the $Ce_{0.75}Zr_{0.25}O_2$ solid solution (28.871°, PDF 00-028-0271), where complete substitution of larger Ce^{4+} ions (0.097 nm) [36] with smaller Zr^{4+} ions (0.084 nm) [20] occurred, maintaining the FCC cubic structure. Consequently, effective incorporation of the Zr^{4+} cations into the CeO_2 lattice can be assumed for the CeZr EG supports. Broad reflections of the CeZr EG support prevent identification of the coexistence of tetragonal ZrO_2 phase (PDF 01-081-1545), which exhibits characteristic diffraction maxima in their direct vicinity.

In the case of CeZr HT supports, diffraction reflections exhibited tailing and much narrower and intense peaks (Fig. 3). Shift of the characteristic 2θ positions is not considerably pronounced with

respect to the FCC CeO_2 standard (PDF 00-034-0394), which indicates less effective Zr^{4+} incorporation into the CeO_2 lattice. Peak tailing on the other hand reveals coexistence of separate tetragonal (t-ZrO_2) crystalline phase. The close vicinity and consequential overlap of low intensity t-ZrO_2 and FCC CeO_2 reflections makes the identification of low concentration segregated ZrO_2 rich phases from the XRD profile debatable. For an univocal identification of the CeZr structural phases, luminescence study using a structural probe could be applied [37].

3.2. NiCo bimetallic catalysts

Deposition of 3–18 wt.% of nickel and cobalt resulted in a substantial decrease of the specific surface area, which in the case of EG and HT synthesis methods settled between 35.5–40.4 m^2/g and 29.7–44.1 m^2/g, respectively (Table 2). Samples denoted 'before reaction' were subjected to calcination (4 h at 400 °C) to mineralize the CeZr support, followed by calcination (4 h at 650 °C) after NiCo deposition.

SEM characterization of fresh NiCo EG catalysts (Fig. 4) revealed distinctly different morphology of the 3NiCo EG sample compared to all the others with a higher NiCo loading. Nickel and cobalt were finely dispersed over the nanocrystalline support, whereas only few round NiCo particles of approximately 15 nm could be identified using SEM microscopy. Dispersion of nickel and cobalt measured using CO chemisorption (Table 2) supports the SEM observations of 3NiCo EG catalyst, with the value of 16.9%, which corresponds to a diameter of 5.9 nm if round particles are assumed. High specific surface area of the CeZr EG support (120.9 m^2/g) can accommodate only limited loadings of nickel and cobalt, which can also partly incorporate into the mixed oxide support during high-temperature calcination [38]. When total active metal loading was increased to 6 wt.% and above (Fig. 4b–d), the morphology of nickel–cobalt phase changed drastically, leading to dendritic, needle-like elongated structures, some 50–100 nm in diameter and up to 1 μm in length. Some elongated NiCo structures appeared to originate from the CeZr support with the rest stacked over each other, leading to a poor interaction with the CeZr support. A progressive increase of NiCo loading led to thicker NiCo dendrites.

NiCo bimetallic phase was present in the 3NiCo HT catalyst in the form of elongated dendritic particles deposited over the CeZr support, which is fundamentally different to 3NiCo EG sample, where only finely dispersed NiCo phase was present. We believe the considerably lower surface area of the CeZr HT support (120.9 and 66 m^2/g for CeZr EG and CeZr HT, respectively, Table 1) was not able to accommodate finely dispersed NiCo particles at the lowest loading of 3 wt.%, which resulted in poorly dispersed NiCo phase (dispersion value of 4.9%), which corresponds to an average NiCo particle diameter of 20 nm. Analogous to NiCo EG catalysts,
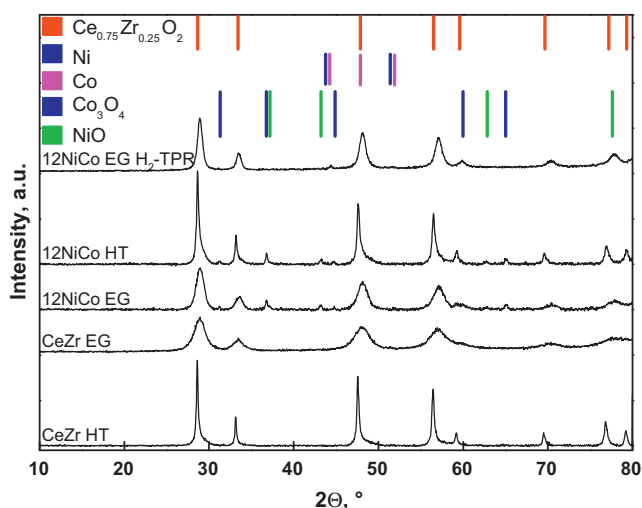

Fig. 3. XRD patterns of 12NiCo EG and 12NiCo HT catalysts and corresponding CeZr EG and CeZr HT supports.

Table 2
Specific surface area before and after reaction and amounts of accumulated carbon during temperature programmed methane dry reforming reaction over various NiCo HT and NiCo EG catalyst samples.

Sample	BET surface area (m²/g)		Accumulated carbon (wt.%)	Dispersion of nickel and cobalt (%)	
	Before reaction	After reaction		Before reaction	After reaction
CeZr EG[a]	120.9	39.1	0.16	/	/
3NiCo EG	38.1	29.1	2.54	16.9 (5.9)	5.4 (18)
3NiCo EG[c]	38.1	44.2	10.42	16.9 (5.9)	4.2 (23)
6NiCo EG	40.4	28.3	2.55	5.9 (17)	2.2 (45)
12NiCo EG	35.5	28.1	5.20	2.1 (47)	1.6 (61)
18NiCo EG	38.1	53.2	38.12	1.5 (65)	1.2 (82)
CeZr HT[b]	66.5	/	/	/	/
3NiCo HT	34.5	69.9	39.11	4.9 (20)	3.2 (31)
6NiCo HT	34.2	35.4	28.22	2.4 (41)	0.5 (196)
12NiCo HT	44.1	30.0	25.99	1.4 (70)	0.6 (163)
18NiCo HT	29.7	35.7	27.32	1.2 (82)	1.4 (70)

Values in parentheses represent the active bimetallic particle size in nm, using calculation from Fan et al. [45].

[a] EG represents the CeZr mixed oxide aged 3.3 h at 180 °C.
[b] HT represents the CeZr mixed oxide aged 6 h at 120 °C.
[c] After stability test at 550 °C.

increasing the NiCo loading in the NiCo HT catalysts led to a thicker layer of stacked NiCo dendrites over the CeZr support (Fig. 5) and continuously lower active metal dispersion values.

XRD analysis of catalysts containing 3 and 6 wt.% of Ni and Co, could not provide any diffraction maxima belonging to ordered phases other than FCC CeO_2, very likely as a result of their low loading and amorphous structure. XRD patterns of 12NiCo EG and 12NiCo HT catalysts are depicted in Fig. 3. They exhibited diffraction patterns, which were weak and diffuse and could be ascribed to NiO and Co_3O_4.

By applying the Scherrer equation to the diffraction peak located at 28.7°, the corresponding CeO_2 crystallite size was calculated to be equal to 7.6 and 35 nm for 12NiCo EG and 12NiCo HT solids, respectively. The calculated growth of the CeO_2 crystallite size of the 12NiCo EG catalyst is consistent with the pronounced decrease of its surface area before and after impregnation (from 120.9 to

35.5 m²/g) as a result of sintering, induced by catalyst thermal stabilization at 650 °C. The increase of CeO_2 crystallite size of 12NiCo HT catalyst was negligible, which is in accordance with a much smaller drop of specific surface area after active metal deposition and calcinations (Tables 1 and 2).

SEM characterization of catalyst samples after temperature programmed reduction (catalyst activation in H_2 containing atmosphere was performed in situ directly prior to all the catalytic tests in order to transform nickel and cobalt oxides into metallic phase, which is active in the investigated methane dry reforming reaction) revealed restructuring of the dendritic NiCo phase into highly polydisperse round particles. The size of the round NiCo particles increased with active metal loading from 20 to 70 nm (6NiCo catalysts) to 100–300 nm (18NiCo catalysts). Active metal particle diameters calculated using CO chemisorption values over reduced NiCo catalysts is consistent with SEM micrographs (Fig. 4).
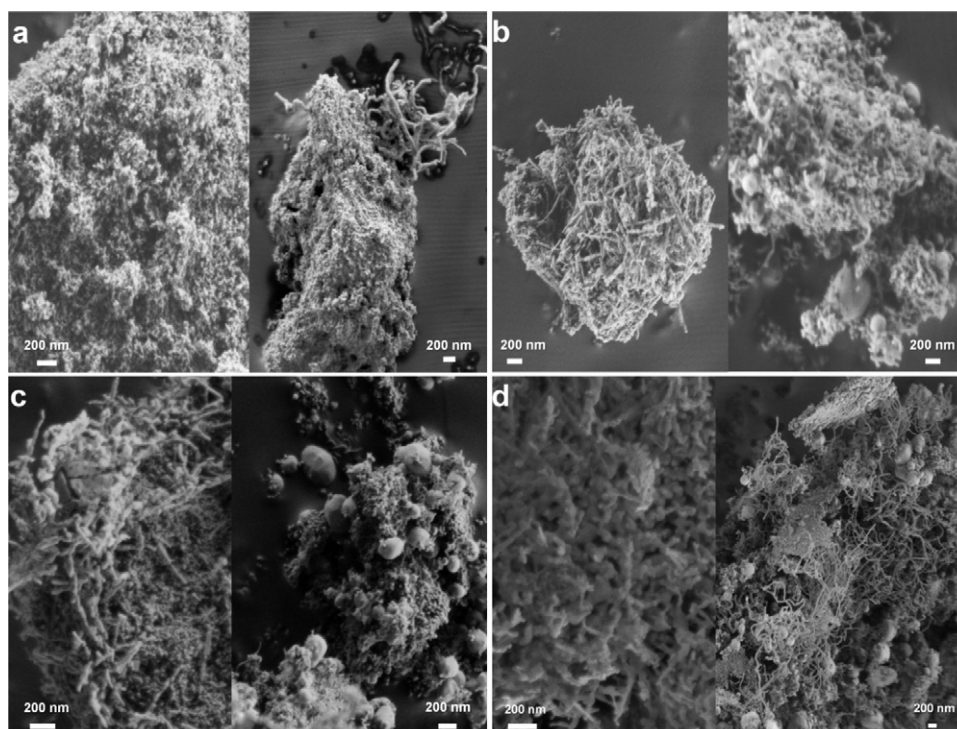

Fig. 4. SEM micrographs of NiCo EG catalysts before and after temperature programmed activity test: (a) 3NiCo EG, (b) 6NiCo EG, (c) 12NiCo EG and (d) 18NiCo EG.
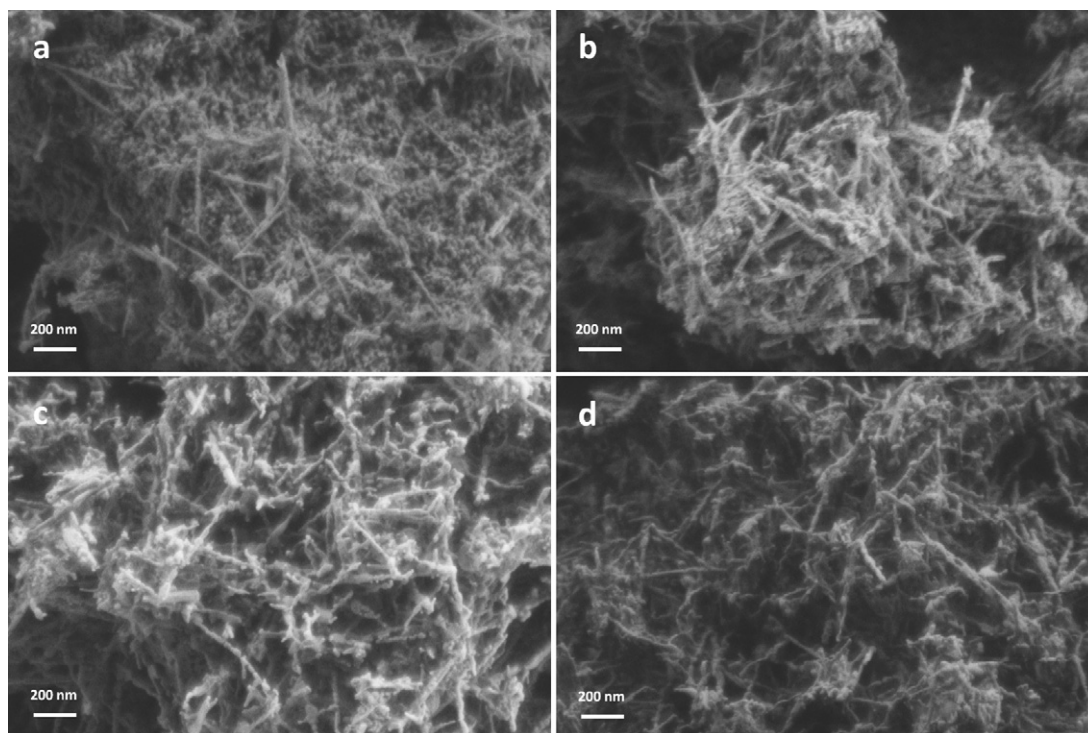
Fig. 5. SEM micrographs of calcined NiCo HT catalysts before temperature programmed activity test: (a) 3NiCo HT, (b) 6NiCo HT, (c) 12NiCo HT and (d) 18NiCo HT.

Exposure of NiCo catalysts to diluted H_2 atmosphere at elevated temperatures caused the formation of a homogeneous alloy between nickel and cobalt, which is crucial for slowing down the carbon accumulation process during methane dry reforming [17]. XRD characterization of reduced 12NiCo EG catalyst did not exhibit any diffraction maxima, which could be ascribed to NiO or Co_3O_4, but exclusively to metallic nickel and cobalt (Fig. 3).

3.3. CH_4–CO_2 reforming performance of NiCo bimetallic catalysts

In the absence of a catalyst, the blank runs with SiC sand and quartz wool achieved conversion of methane below 1% at 800 °C. Consequently, the contribution of reactor setup and gas phase reaction can be proclaimed negligible under the employed conditions.

During testing of bimetallic NiCo catalysts, it was discovered that H_2 addition (5 Nml/min to the CH_4/CO_2 mixture) to initialize the reaction at 500 °C is crucial, since the surface of nickel and cobalt needs to be retained in a reduced, metallic state. Avoiding this step led to oxidation of NiCo particles with H_2O, formed as a result of co-occurring RWGS reaction (Eq. (2)), which caused an instantaneous and complete deactivation of tested catalysts. Hydrogen co-feeding was stopped after about 10 min, when stable catalyst performance was achieved and H_2 concentration from the methane dry reforming reaction was sufficient to sustain the metallic state of NiCo nanoparticles. All successive temperature increments did not require this intervention, since the catalyst produced enough hydrogen to maintain a reductive atmosphere and avoid active metal oxidation. Cobalt oxidation was reported previously for causing catalyst deactivation during the investigated methane reforming reaction using titania supported Ni–Co bimetallic catalysts [17]. H_2-TPR analysis was performed on the catalyst after the initial reaction temperature step, which showed a considerable consumption of hydrogen at around 400 °C, characteristic for the reduction of nickel and cobalt oxides. This confirms the occurrence of catalyst deactivation by oxidation.

Despite feeding of equimolar amounts of methane and carbon dioxide and 1 to 1 stoichiometry of methane dry reforming reaction, CO_2 conversion was higher compared to conversion of CH_4 during the whole tested temperature range for all the catalysts. Co-occurrence of reverse water–gas shift reaction (Eq. (2)) consumed additional amounts of CO_2 (and H_2) to yield CO and water. This negatively influenced the H_2 yield and resulted in a H_2/CO ratio well below the thermodynamically predicted values [12].

Methane and CO_2 conversions as a function of reaction temperature for the 3NiCo EG and 3NiCo HT catalysts are depicted in Fig. 6. Catalytic performance of the bare CeZr EG support is presented for comparison. Substantial boost of catalyst performance after active metal deposition revealed that the catalytic activity predominantly originates from nickel and cobalt, which possess the capability of methane decomposition [39]. The 3NiCo EG catalyst enabled stable activity at temperatures up to 600 °C with deactivation becoming increasingly more prominent at further temperature increments. During the test of 3NiCo HT and 18NiCo HT catalysts (Figs. 6a and 9), reactor plugging by the accumulated carbon occurred at the reaction temperature of 650 °C, leading to a premature end of experiment.

Results of the isothermal test performed using 3NiCo EG catalyst are presented in Fig. 6b. During the performed test, a slow but continuous deactivation with time on stream was observed with CH_4 and CO_2 conversions decreasing from the initial values of 20 and 28% to 8 and 17%, respectively. The H_2/CO ratio also decreased continuously from 0.55 to 0.43. DTG-TPO characterization of the spent catalyst revealed 10.42 wt.% of C accumulated during the experiment, which is in more detailed described in Section 3.4.

During temperature programmed activity tests of 6NiCo EG, 12NiCo EG and 18NiCo EG catalysts (Figs. 7–9), continuous deactivation with time on stream was observed, which was less pronounced for catalyst with a higher active metal content. This is probably a consequence of larger NiCo bimetallic particles present in the 12NiCo EG and 18NiCo EG samples, which are consequently less prone to sintering-induced deactivation. Measured
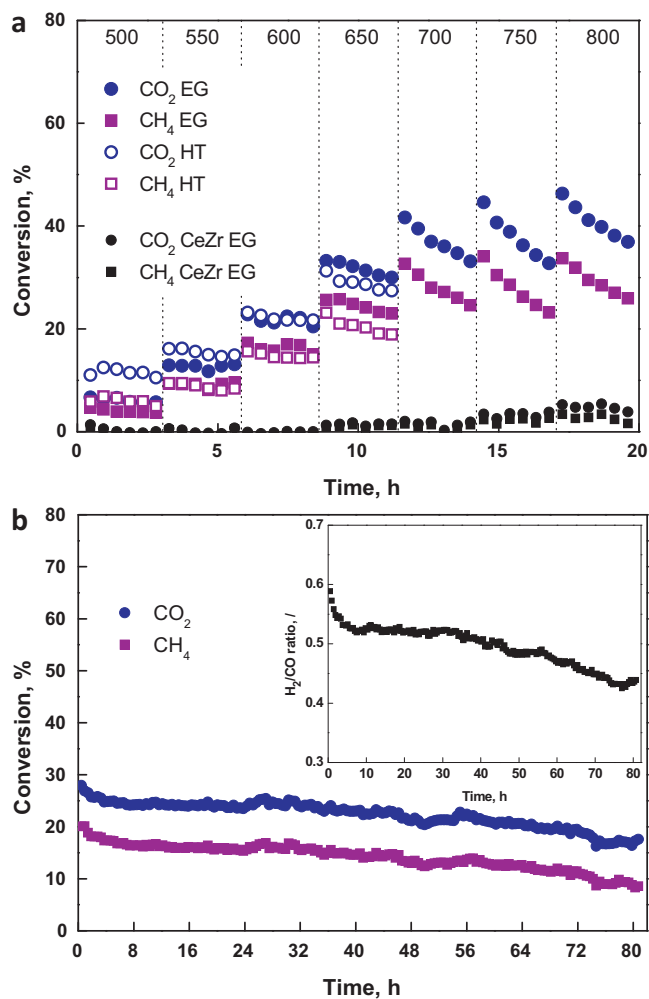
Fig. 6. (a) CH_4 and CO_2 conversion as a function of temperature for CeZr EG support, 3NiCo EG and 3NiCo HT catalysts; (b) isothermal test of 3NiCo EG catalyst conducted at 550 °C.

NiCo dispersion values of catalysts before and after temperature programmed activity tests (Table 2) support this prediction, since the largest drop of metal dispersion was measured for catalysts with finely dispersed NiCo active phase. Contrary to the behavior
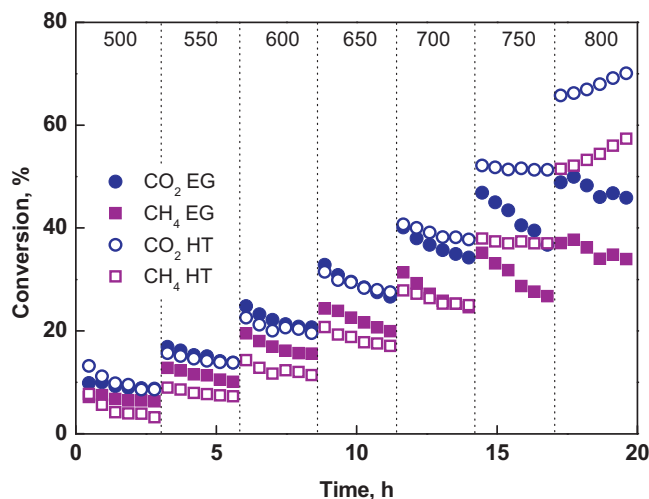

Fig. 7. CH_4 and CO_2 conversion as a function of temperature for 6NiCo EG and 6NiCo HT catalysts.
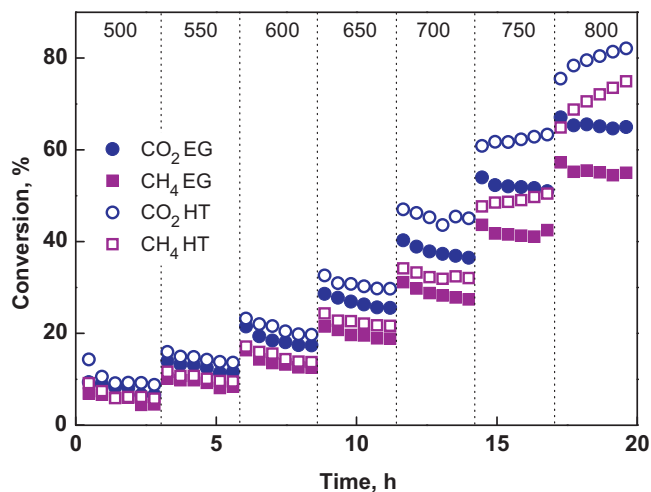
Fig. 8. CH_4 and CO_2 conversion as a function of temperature for 12NiCo EG and 12NiCo HT catalysts.

of NiCo EG catalysts, activity of 6NiCo HT and 12NiCo HT samples stabilized at 750 °C, followed by a continuous increase of catalytic activity at the final temperature increment of 800 °C. Metal dispersion values of the 18NiCo HT catalyst increased slightly, when values from before and after reaction (Table 2) are compared. Extensive growth of carbon nanofilaments during the reaction results in extraction of the NiCo bimetallic particles from the support, possibly leading to newly exposed metal surface, which could result in an apparent increase of metal dispersion.

H_2/CO ratio in the gas stream discharged from the reactor is depicted for all tested NiCo catalysts in Fig. 10. At the initial temperature of 500 °C, the produced H_2/CO ratio varied between 0.3 and 0.4, which increased to 0.45–0.51 for carbon resistant catalysts (3NiCo EG and 6NiCo EG) and to 0.67–0.79 for carbon accumulating catalysts (12NiCo EG and 18NiCo EG, 6 NiCo HT and 12NiCo HT) at 800 °C (Table 2).

The observed divergence in the H_2/CO ratios, obtained over carbon-resistant and carbon-accumulating catalysts indicated a substantial difference in reaction pathway, occurring over these catalysts at temperatures of 700 °C and above.

Correlation between unusually high H_2/CO ratio and greatly accelerated carbon accumulation was observed previously by Nagai
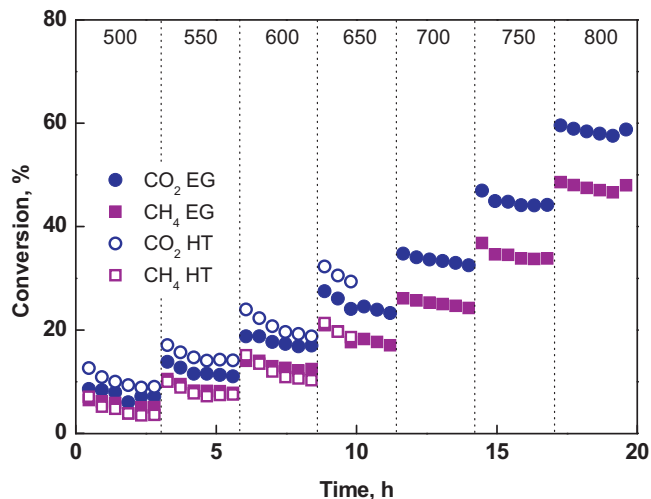

Fig. 9. CH_4 and CO_2 conversion as a function of temperature for 18NiCo EG and 18NiCo HT catalysts.
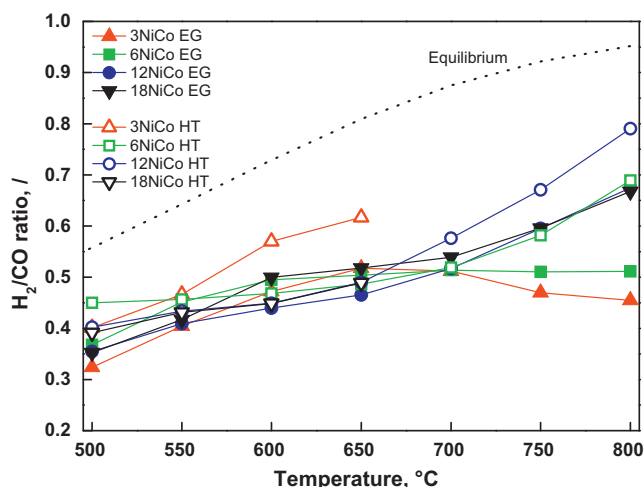
Fig. 10. H_2/CO ratio as a function of reaction temperature for NiCo EG and NiCo HT catalysts.
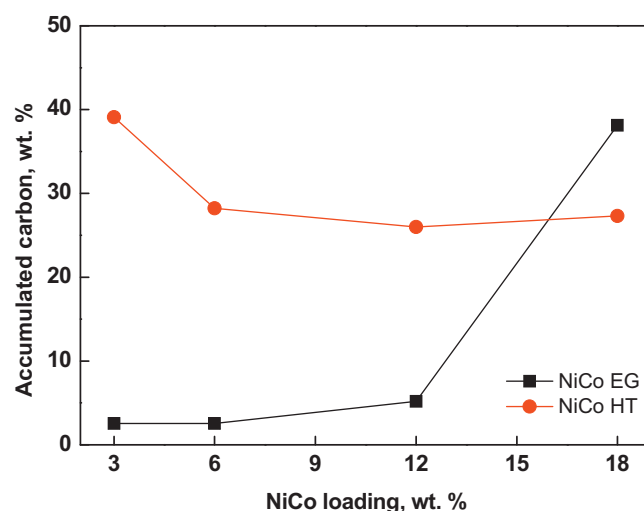

Fig. 11. Amount of accumulated carbon over various NiCo catalysts as a function of active metal loading during temperature programmed activity tests.

et al. [40] over 2% Rh/Al_2O_3 and 4% Rh/CeO_2 catalysts at 600 °C; they attributed this phenomenon to both CO disproportionation and methane dehydrogenation reactions. Considering that major divergence in H_2/CO ratio between carbon-resistant and carbon-accumulating NiCo catalysts, tested in this work occurred at temperatures above 700 °C (Fig. 10), the CO disproportionation reaction is unlikely the primary cause, since this reaction is thermodynamically prohibited at these conditions [9]. On the other hand, methane decomposition reaction (Eq. (3)) is thermodynamically more favorable and also supports a faster increase of CH_4 conversion, compared to conversion of CO_2. This can be observed in Figs. 7 and 8 for NiCo HT catalysts examined at 800 °C.

$$CH_4 \leftrightarrow C + 2H_2, \quad \Delta H°_{298\,K} = 75\,kJ/mol \qquad (3)$$
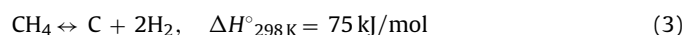
Since methane decomposition does not require CO_2 as a co-reactant and yields 2 moles of H_2 per mole of dehydrogenated methane, promotion of this reaction (Eq. (3)) would positively influence the observed increase of H_2/CO ratio.

Ceria and its oxygen mobility are reported to play a central role in eliminating CH_x fragments (formed over active metal surface during methane dissociation), with spillover of oxygen species, originating from dissociation of CO_2 over its surface (yielding CO and eliminating oxygen vacancies with generated oxygen species) [41–43]. Active sites for fast and effective dissociation of CO_2 can consequently be correlated to the abundance of oxygen vacancies. In order to allow carbon species, covering the active metal surface to react with oxygen species (derived from dissociated CO_2) and thus replenishing oxygen vacancies, the metal–support interface must be extensive, which can be assured with small and well dispersed metal particles [44]. These authors propose the NiCo bimetal particle size to be smaller than 20 nm for effective carbon removal. These postulations can be effectively applied also to ceria–zirconia supported NiCo catalysts, tested in this work.

Over the 3NiCo EG and 6NiCo EG catalysts which exhibited high oxygen mobility and good interaction between NiCo and CeZr phases due to small metallic particle size (calculated diameter of bimetallic particles was 5.9 and 17 nm, respectively), carbon gasification via CO_2 dissociation and oxygen spillover to NiCo phase was timely and efficient, leading to low carbon accumulation. As the active metallic particle size increased with 12 and 18 wt.% active metal loading (47 and 65 nm, respectively), the carbon gasification process became progressively less efficient, leading to a more pronounced carbon accumulation.

On the other hand, over all NiCo HT catalysts (regardless of NiCo loading and consequently size of the active bimetallic particles), the lagging oxygen mobility is not capable of supplying sufficient flux of oxygen species to prevent carbon accumulation. Consequently, all catalysts from this series suffer extensive carbon accumulation (the latter being most pronounced for the 3NiCo HT catalyst sample) and provide no perspective for effective long-term use.

3.4. Coking characteristics of NiCo bimetallic catalysts

Total amounts of carbon accumulated during temperature-programmed methane dry reforming tests are for NiCo EG and NiCo HT catalysts presented in Fig. 11 and Table 2. Among NiCo EG catalysts, a clear correlation between increasing NiCo content and faster carbon accumulation can be observed. During testing of NiCo HT catalysts, carbon accumulation was most pronounced over the 3 wt.% catalyst, which resulted in a premature end of the temperature programmed activity test due to reactor plugging. Carbon deposition over the remaining NiCo HT catalysts was very similar, between 25.99 and 28.22 wt.%, which is substantially higher compared to analogous NiCo EG samples.

When comparing the deactivation rates of NiCo EG catalysts (Figs. 6–9) and amounts of accumulated carbon over these materials, it can be observed that catalysts with a higher NiCo content (above 6 wt.%) enabled relatively stable performance, but also accumulated more carbon (Fig. 11).

Furthermore, when comparing the performance of analogous NiCo EG and NiCo HT catalysts, the latter accumulated considerably more carbon, but their catalytic activity in terms of methane and CO_2 conversion was very similar. This is in accordance with results of San-José-Alonso et al. [46], who report that filamentous carbon accumulation has little effect on deactivation, since the active metallic particles are still in contact with the gas phase and can further perform an active role in the catalytic reaction. Horváth et al. [20] also found no straightforward correlation between catalytic activity and the amount of surface carbon formed on their bimetallic NiRh and NiCo catalysts, dispersed over CeO_2–ZrO_2 oxide support.

In order to reveal the morphology of carbon deposits over NiCo bimetallic catalysts used in temperature programmed activity tests, SEM microscopy was applied. This technique revealed only filamentous carbon on all the tested catalysts. Tortuous filaments were 10–20 nm in diameter and up to 1 μm in length (see right handside
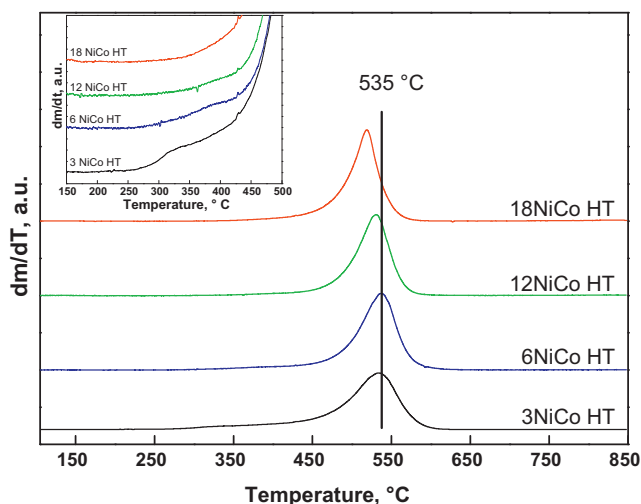
Fig. 12. DTG-TPO profiles of NiCo HT catalysts after temperature programmed methane dry reforming reaction.

of Figs. 4a–d). No other carbon morphologies could be identified using SEM technique.

A more detailed analysis of carbon deposits was performed using DTG-TPO method (curves in Figs. 12 and 13 are offset vertically for clarity).

The measured DTG-TPO profiles over spent 12NiCo HT and 18NiCo HT catalysts confirmed the presence of only one type of carbon, oxidation of which took place in a wide temperature range between 400 and 600 °C. For the 6NiCo HT catalyst, a slight shoulder at around 350 °C could be distinguished, which was more pronounced in the 3NiCo HT catalyst.

A general agreement on the oxidation progress of specific carbon morphologies is the following: more reactive amorphous carbon is oxidized first, at around 300 °C, followed by oxidation of crystalline carbon at temperatures above 500 °C [47–49].

Oxidation of carbon deposits over spent NiCo EG catalysts containing 6–18 wt.% active metal content occurred in the temperature range similar to NiCo HT catalysts, between 400 and 600 °C (Fig. 13). Temperature of carbon oxidation, as well as SEM microscopy results are characteristic of nanofibrous carbon.

San-José-Alonso et al. [46] identified filament-type carbon over their NiCo/γ-Al$_2$O$_3$ catalysts, oxidation of which took place at
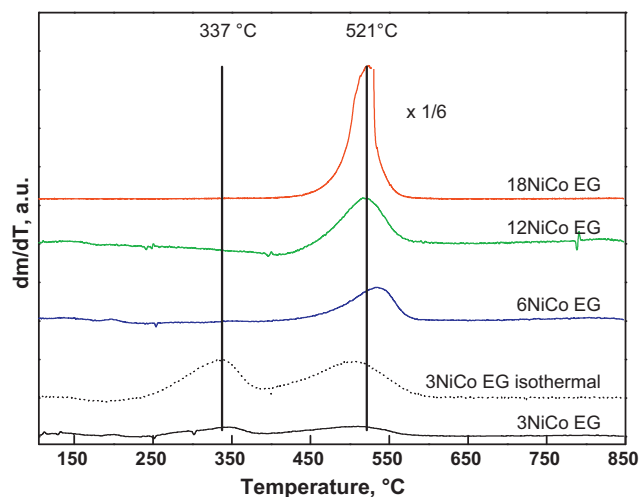

Fig. 13. DTG-TPO profiles of NiCo EG catalysts after temperature programmed methane dry reforming reaction.

around 560 °C. This corresponds closely to the DTG-TPO results obtained in this study, where SEM characterization revealed filamentous carbon deposits which were oxidized at slightly lower temperatures (around 520–535 °C). Discrepancies between our results and the ones obtained by San-José-Alonso et al. [46] are likely connected to high oxygen mobility of the CeZr support, which enables facile spillover of oxygen atoms to initiate the carbon oxidation process, compared to Al$_2$O$_3$, which does not support this mechanism. This would also explain why oxidation of carbon deposits over NiCo EG catalysts with more pronounced oxygen mobility occurred about 15 °C earlier compared to chemically identical NiCo HT catalysts (Figs. 12 and 13).

The most noticeable deviation in DTG-TPO results was observed during the analysis of 3NiCo EG catalyst, where two well-separated oxidation peaks were observed, the first one centered at 342 °C and the second one at 509 °C. The first peak contributed to 41% and the second peak to 59% of the total carbon mass. This indicates an additional type of carbon accumulated over this material, which was absent in all the other tested samples, except in minor quantities in 3NiCo HT catalyst (inset in Fig. 12). Since only catalysts with the lowest active metal loading (and consequently smallest active metal particle size) accumulated two distinct types of carbon, formation of easily oxidized carbon is probably limited to specific active metal morphology. During TPO analysis of Ni–Co–Ce–Zr catalysts, Horváth et al. [20] identified two carbon oxidation peaks at 350 and 500 °C. Furthermore, they observed that the ratio of both peaks changed progressively in favor of the high temperature one during alternating cycles of carbon deposition (via methane dry reforming reaction) and its oxidation (with TPO). The observed shift was ascribed to alteration of catalyst structure during high temperature exposure with consequent changes in structure of deposited carbon.

Total amount of deposited carbon in the 3NiCo EG catalyst during the temperature programmed activity test was the lowest among all, 2.54 wt.%, which is probably connected to highest dispersion of NiCo phase among all tested catalyst samples. Lower NiCo loadings can be more efficiently dispersed over the CeZr support, enabling a more intimate contact and leading to a more efficient oxidation of carbon deposits via activated oxygen species spillover [50,51]. To make this mechanism plausible, CeZr support must exhibit high oxygen mobility, as in the case with EG catalysts (Table 1). Similar conclusions were drawn also by others, such as Zhang et al. [9], who attributed deactivation of their Ni–Cu, Ni–Fe and Ni–Mn to carbon fouling, but not their Ni–Co bimetallic catalysts during the 28 h screening test. They report no carbon deposition over bimetallic Ni–Co catalysts with an 8.5 wt.% active metal content as a result of their higher metal dispersion. Higher coking resistance of minute NiCo entities is reported to originate from the following reasons: (i) initiation of coking requires a minimal number of nickel atoms in the ensemble, which is not met in the smallest particles [52–54] and (ii) stronger electronic interactions between the catalyst support and finely dispersed metallic nanoparticles [55].

The 3NiCo EG catalyst exhibited most effective resistance to carbon accumulation during the temperature programmed activity tests. This solid was further subjected to isothermal tests at 550 (Fig. 6b) and 750 °C (results not shown) in order to more accurately determine the temperature range, where each carbon type is highly promoted and possibly reveal the reaction pathway, responsible for catalyst fouling.

Characterization of spent 3NiCo EG catalyst after separate isothermal tests at 550 and 750 °C revealed 10.42 and 0.23 wt.% of deposited carbon, respectively. This test clearly demonstrated that carbon accumulation occurs only at low reaction temperatures.

Among the multitude of co-occurring reactions during methane dry reforming process [56], those very probably responsible for
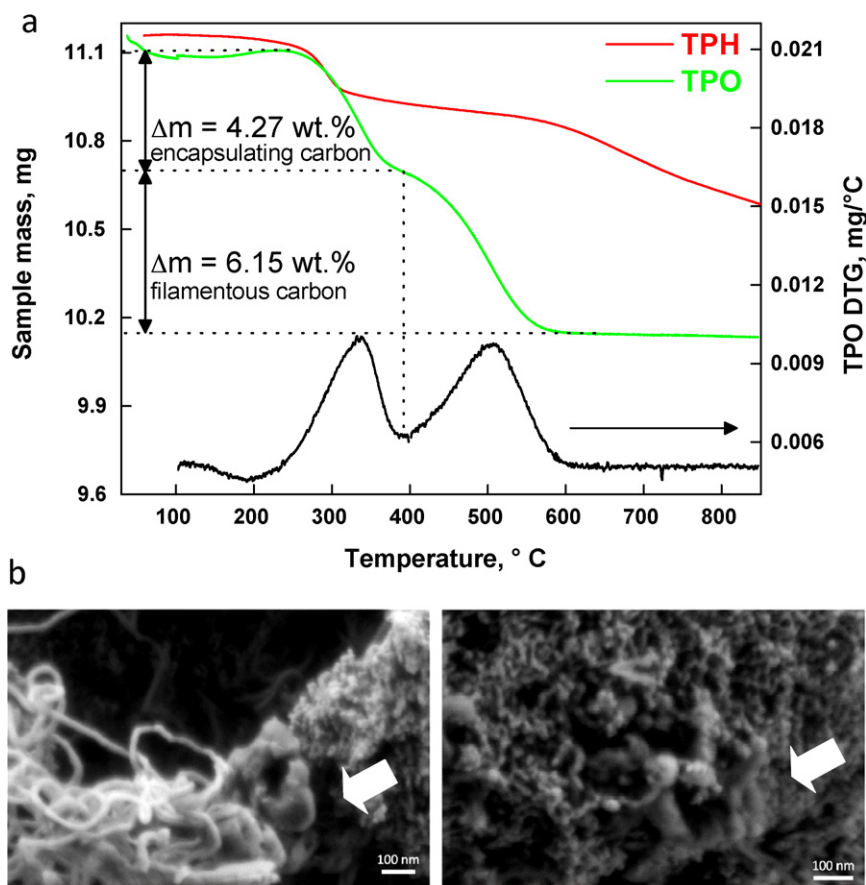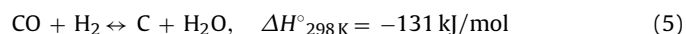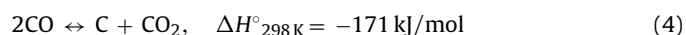
Fig. 14. (a) TPO and TPH of carbon deposits formed during the 80 h isothermal test at 550 °C and (b) SEM micrographs of 3NiCo EG catalyst depicting areas of encapsulating and whisker type carbon deposited during the 80 h isothermal test at 550 °C.

low-temperature carbon accumulation are CO disproportionation (Boudouard reaction (Eq. (4)) and reverse carbon gasification reaction (Eq. (5)), which are exothermic and consequently thermodynamically forbidden at temperatures above 550 °C [9,56].

$$2CO \leftrightarrow C + CO_2, \quad \Delta H°_{298\,K} = -171\,kJ/mol \qquad (4)$$

$$CO + H_2 \leftrightarrow C + H_2O, \quad \Delta H°_{298\,K} = -131\,kJ/mol \qquad (5)$$

DTG-TPO characterization revealed two types of carbon deposits over the 3NiCo EG catalyst after the isothermal test at 550 °C (Fig. 14a). The first peak was centered at around 337 °C contributing to 41% and the second peak centered at around 506 °C contributing to 59% of total carbon accumulation. This is remarkably similar to the DTG-TPO characterization results, obtained over spent 3NiCo EG catalyst after the temperature programmed activity test (Fig. 13).

Carbon gasification using temperature programmed hydrogenation (TPH) technique was also attempted for identification/quantification of different types of carbon deposits. In addition, this method was investigated as a possible in situ catalyst regeneration procedure. As can be seen in Fig. 14a, carbon gasification using 10% H₂/N₂ atmosphere was substantially less efficient, with only about 50% of carbon deposits removed at temperatures up to 850° C, making the characterization of carbon deposits impossible.

SEM characterization of 3NiCo EG catalyst after the isothermal test at 550 °C confirmed that contrary to all other investigated catalyst samples, patches of catalyst surface apparently covered by encapsulating carbon were identified (Fig. 14b). The presence of encapsulating carbon in noticeable quantities (41% of 10.42 wt.%,

as identified by DTG-TPO) could be responsible for the continuous catalytic deactivation, as is depicted in Fig. 6b.

BET surface area of 3NiCo EG catalyst before and after stability test at 550 °C revealed an increase from 38.1 to 44.2 m²/g (Table 2), which is a consequence of accumulation of fibrous carbon. Higher BET specific surface area of spent catalysts, compared to fresh calcined samples was observed also for other carbon accumulating catalysts (NiCo HT) during temperature programmed activity tests. Specific surface area of carbon nanofilaments is according to literature data roughly 215 m²/g [57], which is considerably higher than the fresh calcined NiCo catalysts (29.7–44.1 m²/g). Consequently, substantial carbon accumulation will result in an actual increase of the specific surface area despite catalyst sintering. Carbon removal by oxidation would result in a decrease of the specific surface area of spent catalyst samples, since its contribution would be annulled, leaving only the contribution of thermally stabilized NiCo/CeZr catalytic material.

By combining the observations, obtained during the temperature programmed and isothermal tests at 550 and 750 °C with 3NiCo EG catalyst, two important facts were disclosed: (i) catalyst coking occurs only in the lower range of operating temperatures; (ii) carbon formed during the initial stages of temperature programmed reforming is not gasified at subsequent higher operating temperatures. It must be stated here that only 3NiCo EG catalyst (and possibly 6NiCo EG) is included in this conclusion, because all other tested catalysts exhibited high carbon accumulation rates, which do not provide prospects for possible long-term use without eventual reactor plugging.

In order to prevent carbon accumulation and enable long-term stable performance over NiCo bimetallic catalysts in the methane

dry reforming reaction, the following conditions need to be fulfilled simultaneously: (i) high oxygen mobility within the CeZr support, encouraged by small crystallite size and highly defective CeO_2 crystallite lattice must be provided via the appropriate synthesis method to enable timely oxidation of carbon deposits; (ii) NiCo particles must be highly dispersed in order to assure a large interface and strong interaction between active metal and support, for effective spillover of oxygen species; (iii) reforming temperatures below 600 °C should not be used, since carbon accumulating CO disproportionation and reverse carbon gasification reactions are highly promoted.

4. Conclusion

Synthesis of nanocrystalline CeZr solid solutions via EG and HT methods resulted in morphologically substantially different products, despite identical chemical composition. EG method produced powders with highly defective crystalline structure, BET specific surface area up to 121 m^2/g and superior oxygen mobility, compared to CeZr HT powders. By increasing the loading of nickel and cobalt as active metals from 3 to 18 wt.%, a progressive decrease in metal dispersion was measured. Within the tested temperature range, the calculated H_2/CO ratio was between 0.4 and 0.79 that was considerably influenced by the reverse water–gas shift reaction. Higher H_2/CO ratios were characteristic of non-perspective carbon accumulating catalysts as a result of accelerated methane decomposition reaction at reaction temperatures above 700 °C.

In order to minimize carbon accumulation and enable long-term performance over NiCo bimetallic catalysts, nickel and cobalt loadings of 6 wt.% and above should be omitted, since they cause active metal phase segregation in the form of round particles, larger than 50 nm, which results in lower interaction with the CeZr support. Growth of carbon nanofilaments over the catalyst does not lead to deactivation, but can cause reactor plugging.

High oxygen mobility within the CeZr support, originating from small crystallite size and highly defective CeO_2 crystallite lattice, must be provided via the appropriate synthesis conditions. Oxygen mobility plays a vital role in gasification of carbonaceous deposits with spillover of oxygen species, originating from dissociation of CO_2 over CeZr surface. In combination with low NiCo loadings to assure a large interface and strong interaction between active metal and support, long-term reforming of undiluted equimolar CH_4–CO_2 streams can be achieved.

Acknowledgement

References

[1] D. Deublein, A. Steinhauser, Biogas from Waste and Renewable Resources, Wiley, Weinheim, 2008.
[2] 2011 AEBIOM Annual Statistical Report.
[3] S. Cavenati, C.A. Grande, A.E. Rodrigues, Chemical Engineering Science 61 (2006) 3893–3906.
[4] D. Thrän, M. Seiffert, F. Müller-Langer, A. Plättner, A. Vogel, Möglichkeiten einer Europäischen Einspeisungsstrategie, Institut für Energie und Umwelt, Leipzig, Germany, 2007.
[5] J. Rostrup-Nielsen, L.J. Christiansen, Concepts in Syngas Manufacture, Imperial College Press, London, 2011, ISBN 978-1-84816-568-7.
[6] A.T. Ashcroft, A.K. Cheetham, J.S. Foord, M.L.H. Green, C.P. Grey, A.J. Murrell, P.D.F. Vernon, Nature 344 (6264) (1990) 319–321.
[7] D. Wilhelm, D. Simbeck, A. Karp, R. Dickenson, Fuel Processing Technology 71 (2001) 139–148.
[8] M.C.J. Bradford, M.A. Vannice, Catalysis Reviews: Science and Engineering 41 (1999) 1–42.
[9] J. Zhang, H. Wang, A.K. Dalai, Journal of Catalysis 249 (2007) 300–310.
[10] S.T. Oyama, P. Hacarlioglu, Y. Gu, D. Lee, International journal of Hydrogen Energy 37 (2012) 10444–10450.
[11] P. Djinović, J. Batista, A. Pintar, International Journal of Hydrogen Energy 37 (2012) 2699–2707.
[12] P. Djinović, I.G. Osojnik Črnivec, J. Batista, J. Levec, A. Pintar, Chemical Engineering and Processing 50 (2011) 1054–1062.
[13] J.R. Rostrup Nielsen, J.H.B. Hansen, Journal of Catalysis 144 (1993) 38–49.
[14] P. Ferreira-Aparicio, A. Guerrero-Ruiz, I. Rodriguez-Ramos, Applied Catalysis A 170 (1998) 177–187.
[15] K. Nagaoka, M. Okamura, K.-I. Aika, Catalysis Communications 2 (2001) 255–260.
[16] Z. Hou, O. Yokota, T. Tanaka, T. Yashima, Applied Surface Science 233 (2004) 58–68.
[17] K. Takanabe, K. Nagaoka, K. Nariai, K.-I. Aika, Journal of Catalysis 232 (2005) 268–275.
[18] E. Nikolla, J. Schwank, S. Linic, Journal of Catalysis 263 (2009) 220–227.
[19] M. Rezaei, S.M. Alavi, S. Sahebdelfar, P. Bai, X. Liu, Z.-F. Yan, Applied Catalysis B 77 (2008) 346–354.
[20] A. Horváth, G. Stefler, O. Geszti, A. Kienneman, A. Pietraszek, L. Guczi, Catalysis Today 169 (2011) 102–111.
[21] B.M. Nagaraja, D.A. Bulushev, S. Beloshapkin, J.R.H. Ross, Catalysis Today 178 (2011) 132–136.
[22] H.S. Bengaard, I. Alstrup, I. Chorkendorff, S. Ullmann, J.R. Rostrup-Nielsen, J.K. Nørskov, Journal of Catalysis 187 (1999) 238–244.
[23] Z. Hou, O. Yokota, T. Tanaka, T. Yashima, Applied Catalysis A 253 (2003) 381–387.
[24] X. Liang, J. Xiao, B. Chen, Y. Li, Inorganic Chemistry 49 (2010) 8188–8190.
[25] K.P. de Jong, Synthesis of Solid Catalysts, Wiley-VCH, Weinheim, 2009.
[26] M. Boaro, M. Vicario, C. de Leitenburg, G. Dolcetti, A. Trovarelli, Catalysis Today 77 (2003) 407–417.
[27] G. Vlaic, R. Di Monte, P. Fornasiero, E. Fonda, J. Kašpar, M. Graziani, Journal of Catalysis 182 (1999) 378–389.
[28] E. Mamontov, T. Egami, R. Brezny, M. Koranne, S. Tyagi, Journal of Physical Chemistry B 104 (2000) 11110–11116.
[29] M. Adamowska, S. Muller, P. Da Costa, P. Burg, A. Krzton, Applied Catalysis B 74 (2007) 278–289.
[30] A. Laachir, V. Perrichon, A. Badri, J. Lamotte, E. Catherine, J.C. Lavalley, J. El Fallah, L. Hilaire, F. Le Normand, E. Quéméré, G.N. Sauvion, O. Touret, Journal of the Chemical Society, Faraday Transactions 87 (1991) 1601–1609.
[31] J. El Fallah, S. Boujana, H. Dexpert, A. Kiennemann, J. Majerus, O. Touret, F. Villain, F. Le Normand, Journal of Physical Chemistry 98 (1994) 5522–5533.
[32] P. Fornasiero, R. Dimonte, G.R. Rao, J. Kašpar, S. Meriani, A. Trovarelli, M. Graziani, Journal of Catalysis 151 (1995) 168–177.
[33] V. Raju, S. Jaenicke, G.K. Chuah, Applied Catalysis B 91 (2009) 92–100.
[34] S. Jaenicke, G.K. Chuah, V. Raju, Y.T. Nie, Catalysis Surveys from Asia 12 (2008) 153–169.
[35] S. Damyanova, B. Pawelec, K. Arishtirova, M.V. Martinez Huerta, J.L.G. Fierro, Applied Catalysis A 337 (2008) 86–96.
[36] M.L. Fu, X.H. Yue, D.Q. Ye, J.H. Ouyang, B.C. Huang, J.H. Wu, H. Liang, Catalysis Today 153 (2010) 125–132.
[37] T. Montini, A. Speghini, L. De Rogatis, B. Lorenzut, M. Bettinelli, M. Graziani, P. Fornasiero, Journal of the American Chemical Society 131 (2009) 13155–13160.
[38] H. Mori, C. Wen, J. Otomo, K. Eguchi, H. Takahashi, Applied Catalysis A 245 (2003) 79–85.
[39] J.M. Wei, E. Iglesia, Journal of Catalysis 224 (2004) 370–383.
[40] M. Nagai, K. Nakahira, Y. Ozawa, Y. Namiki, Y. Suzuki, Chemical Engineering Science 62 (2007) 4998–5000.
[41] N. Laosiripojana, S. Assabumrungrat, Applied Catalysis B 60 (2005) 107–116.
[42] R. Wang, H. Xu, X. Liu, Q. Ge, W. Li, Applied Catalysis A 305 (2006) 204–210.
[43] K. Takanabe, K. Nagaoka, K.-I. Aika, Catalysis Letters 102 (2005) 153–157.
[44] J. Zhang, H. Wang, A.K. Dalai, Applied Catalysis A 339 (2008) 121–129.
[45] M.-S. Fan, A.Z. Abdullah, S. Bhatia, Applied Catalysis B 100 (2010) 365–377.
[46] D. San-José-Alonso, J. Juan-Juan, M.J. Illán-Gómez, M.C. Román-Martínez, Applied Catalysis A 371 (2009) 54–59.
[47] P. Wang, E. Tanabe, K. Ito, J. Jia, H. Morioka, T. Shishido, K. Takehira, Applied Catalysis A 231 (2002) 35–44.
[48] Z. Yu, D. Chen, M. Rønning, B. Tøtdal, T. Vrålstad, E. Ochoa-Fernández, A. Holmen, Applied Catalysis A 338 (2008) 147–158.
[49] J.W. Long, J. Laskoski, T.M. Keller, K.A. Pettigrew, T.N. Zimmerman, S.B. Qadri, G.W. Peterson, Carbon 48 (2010) 501–508.
[50] A.M. Efstathiou, A. Kladi, V.A. Tsipouriari, X.E. Verykios, Journal of Catalysis 158 (1996) 64–75.
[51] H. Song, U.S. Ozkan, Journal of Catalysis 261 (2009) 66–74.
[52] J.R. Rostrup-Nielsen, Journal of Catalysis 33 (1974) 184–201.
[53] T. Osaki, T. Mori, Journal of Catalysis 204 (2001) 89–97.
[54] E. Ruckenstein, H.Y. Wang, Applied Catalysis A 204 (2000) 257–263.
[55] H.S. Roh, H.S. Potdar, K.W. Jun, J.W. Kim, Y.S. Oh, Applied Catalysis A 276 (2004) 231–239.
[56] Y. Cui, H. Zhang, H. Xu, W. Li, Applied Catalysis A 318 (2007) 79–88.
[57] C.D. Taboada, J. Batista, A. Pintar, J. Levec, Applied Catalysis B 89 (2009) 375–382.